

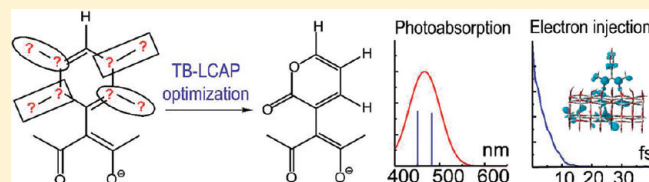
Inverse Design and Synthesis of acac-Coumarin Anchors for Robust TiO₂ Sensitization

Dequan Xiao,* Lauren A. Martini, Robert C. Snoeberger, III, Robert H. Crabtree,* and Victor S. Batista*

Department of Chemistry, Yale University, New Haven, Connecticut 06520-81087, United States

Supporting Information

ABSTRACT: An inverse design methodology suitable to assist the synthesis and optimization of molecular sensitizers for dye-sensitized solar cells is introduced. The method searches for molecular adsorbates with suitable photoabsorption properties through continuous optimization of “alchemical” structures in the vicinity of a reference molecular framework. The approach is illustrated as applied to the design and optimization of linker chromophores for TiO₂ sensitization, using the recently developed phenyl-acetylacetonate (i.e., phenyl-acac) anchor [McNamara et al. *J. Am. Chem. Soc.* **2008**, *130*, 14329–14338] as a reference framework. A novel anchor (3-acac-pyran-2-one) is found to be a local optimum, with improved sensitization properties when compared to phenyl-acac. Its molecular structure is related to known coumarin dyes that could be used as lead chromophore anchors for practical applications in dye-sensitized solar cells. Synthesis and spectroscopic characterization confirms that the linker provides robust attachment to TiO₂, even in aqueous conditions, yielding improved sensitization to solar light and ultrafast interfacial electron injection. The findings are particularly relevant to the design of sensitizers for dye-sensitized solar cells because of the wide variety of structures that are possible but they should be equally useful for other applications such as ligand design for homogeneous catalysis.



1. INTRODUCTION

The design of molecular chromophores is critically important for the development of dye-sensitized solar cells (DSSCs)^{1,2} for photoelectricity generation and photocatalysis.^{3–6} Since the discovery of DSSCs by O’Regan and Grätzel,¹ hundreds of dyes have been developed and tested,^{7–10} and cells with photoconversion efficiencies as high as 11% have been reported.^{1,2,11} However, for almost 20 years, the outstanding challenge remains to be the design of DSSCs with even higher photoconversion efficiencies. This Article introduces an inverse design methodology to guide the synthesis and optimization of lead molecular chromophores with suitable photoabsorption properties. The approach uses a gradient-assisted deterministic search of molecular adsorbates based on a reference molecular structure, in the landscape of “alchemical” molecular frameworks, as described by the tight-binding linear combination of atomic potential (TB-LCAP) Hamiltonian. The method is illustrated specifically by the design of a novel sensitizer, inspired by the recently reported 3-phenyl-acetylacetonate (i.e., phenyl-acac) anchor. The 3-acac-pyran-2-one anion emerges from the optimization process as a local optimum structure, superior to phenyl-acac. The finding is confirmed by the experimental synthesis and spectroscopic characterization.

The search of molecular adsorbates for highly efficient dye-sensitized solar cells is challenging. Most of the work reported to date has been on the basis of direct molecular design using empirical strategies,¹² where typical “guess-and-check” procedures face the challenge of selecting suitable candidates from an immense number of accessible stable molecules, followed by the

synthesis of a large number of molecules for testing.^{13,14} In contrast, inverse design approaches^{15–19} could optimize the search of chemical structures using algorithms based on either discrete¹⁵ or continuous^{16,18} transformations, ideally leading to a greatly improved lead structure. However, such methods have yet to be applied to the design and optimization of sensitizers.

The earliest studies of inverse design methodologies have been focused on finding maximum bandgap atomic configurations using the effective inverse band-structure (IBS) approach,¹⁵ a simulated annealing algorithm for discrete search of atomic superlattices. Later, the IBS approach was implemented in conjunction with a genetic algorithm in search of specific configurations for target band-gaps in quaternary semiconductors.^{20,21} More recently, the linear combination of atomic potential (LCAP) approach was proposed for inverse design at the density functional theory (DFT) level.¹⁶ This method was applied to the search of molecules with optimum polarizabilities and hyperpolarizabilities, as guided by the gradient analysis.¹⁶ In addition, the LCAP approach was expanded into the tight-binding (TB) framework using a Hückel-type Hamiltonian and shown to be effective at locating optimal structures within a large number (10^2 – 10^{16}) of possible chemical structures.²² To avoid getting trapped at local minima of rugged optimization hypersurfaces, the LCAP approach has been augmented by Monte Carlo moves, including the gradient-directed Monte Carlo (GDMC) strategy that introduces “jumps” over barriers defined by discrete

Received: March 5, 2011

Published: May 09, 2011

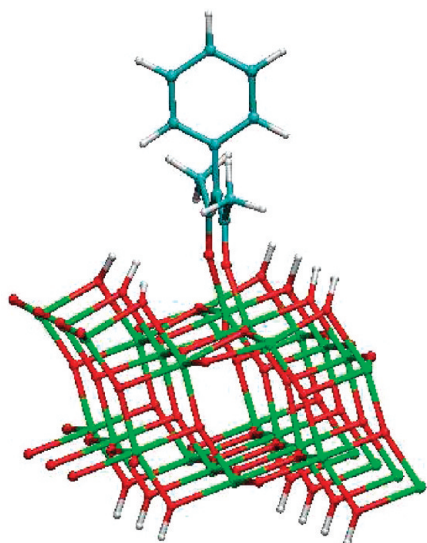


Figure 1. Phenyl-acac linker covalently bound to the 101 surface of a TiO_2 anatase nanoparticle. Color key: C (blue), H (white), O (red), Ti (green).

molecular configurations.^{23,24} The GDMC approach has been applied to the optimization of HOMO–LUMO transitions,²⁴ protein sequence design,²⁵ and protein folding in lattice models of hydrophobic-polar groups.²⁶

This Article introduces the extended-Hückel (EH) generalization of the Hückel TB-LCAP approach²² for the purpose of optimizing solar energy harvesting by molecular sensitizers. Contrary to the Hückel TB-LCAP approach where only π orbitals are included in the description of valence electrons, the EH generalization includes both σ and π orbitals formed by S, P, and D atomic orbitals representing the full valence shell of a wide range of molecular structures. After screening and optimizing at the EH/TB-LCAP level, the visible photoabsorption spectra of the most promising structures are re-evaluated at the time-dependent DFT (TDDFT) level of theory, and the interfacial electron injection dynamics is simulated as in previous work,^{5,6,27–29} to ensure efficient photoconversion of visible light by the processes of photoabsorption and charge injection into TiO_2 .

The phenyl-acac linker is particularly attractive for the sensitization of metal–oxide surfaces because it binds strongly to nanoporous TiO_2 thin films, even in aqueous solutions and under oxidative conditions (Figure 1).⁶ However, its photoabsorption spectrum peaks in the UV region. Therefore, it is important to search for structures with a common binding motif to TiO_2 but with enhanced photoabsorption of solar light leading to interfacial electron injection. Here, we report the successful optimization of the photoabsorption properties through inverse design based on a continuous “alchemical” search of six-membered ring structures, in the vicinity of the phenyl-acac reference molecular framework, as described by the EH/TB-LCAP Hamiltonian.

This Article is organized as follows: Section 2 describes the methods, including the computational algorithm for inverse design, quantum dynamics simulations of interfacial electron injection, calculations of photoabsorption spectra at the TDDFT level, and experimental synthesis and spectroscopic characterization methods. Section 3 presents the results leading to the finding

of 3-acac-pyran-2-one anion as a local optimum structure, superior to phenyl-acac. Comparisons are shown between the predicted and experimentally measured photoabsorption spectra for the synthesized molecular adsorbates. The reported results suggest that 3-acac-pyran-2-one could be used as a lead chromophore to obtain robust dye-sensitizers with more intense visible absorption bands and efficient electron injection on the TiO_2 surface.

2. METHODS

2.1. Extended Hückel/TB-LCAP Hamiltonian. This section outlines the extended-Hückel tight-binding linear combination of the atomic potential (EH/TB-LCAP) method as implemented for optimizing the nature of molecular structures with respect to solar light harvesting. Contrary to the Hückel TB-LCAP approach,²² where only π orbitals are included in the description of valence electrons, the EH/TB-LCAP method includes both σ and π orbitals formed by S, P, and D atomic orbitals. Therefore, the method can describe full valence shell structures of a wide range of molecular structures, including adsorbate molecules covalently attached to metal–oxide surfaces. Promising structures found by the EH/TB-LCAP method are subsequently re-evaluated at the TDDFT level of theory, and the interfacial electron injection dynamics is simulated to assess for ultrafast charge injection into TiO_2 surfaces, as in previous work.^{5,6,27–29}

The extended Hückel approach has been extensively applied for calculations of electronic structures and photoabsorption spectra for a wide range of molecular and solid-state structures,^{30,31} as well as for the studies of sensitized TiO_2 surfaces including the analysis of interfacial electron transfer (IET).^{5,6,27–29} Therefore, its description is limited to its implementation into the TB-LCAP method.

The time-independent Schrödinger equation is represented in matrix form:

$$\mathbf{H}\mathbf{Q} = \mathbf{E}\mathbf{S}\mathbf{Q} \quad (1)$$

where \mathbf{H} is the extended Hückel Hamiltonian in the basis of Slater-type atomic orbitals (STO's), \mathbf{Q} is the matrix of eigenvectors, \mathbf{E} is the diagonal matrix of eigenstate energies, and \mathbf{S} is the overlap matrix of the STO's. The EH/TB-LCAP Hamiltonian is defined in terms of the participation coefficients $\{b_i^{(A)}\}$ for the complete set of atom (or functional group) types A and sites i , giving the probability weight of such an atom type A at site i while undergoing a continuous transformation of each site through N_i^{type} possible atom types. The constraints are $\sum_A^{N_i^{\text{type}}} b_i^{(A)} = 1$ and $0 \leq b_i^{(A)} \leq 1$.

Using the participation coefficients $b_i^{(A)}$, the diagonal matrix elements of the EH/TB-LCAP Hamiltonian are defined as follows:

$$H_{i\alpha, i\alpha} = \sum_{A=1}^{N_i^{\text{type}}} b_i^{(A)} h_{i\alpha, i\alpha}^{(A)} \quad (2)$$

where α represents a STO of atom type A and $h_{i\alpha, i\alpha}^{(A)}$ is the EH diagonal Hamiltonian matrix element for atom type A at site i . Note that for the specific case of $b_i^{(A)} = 1$, $H_{i\alpha, i\alpha} = h_{i\alpha, i\alpha}^{(A)}$ because all other participation coefficients at the i -site are equal to zero. More generally, $H_{i\alpha, i\alpha}$ is an arithmetic average of EH matrix elements associated with all possible atom types at site i weighted by their corresponding participation coefficients. Analogously, the off-diagonal matrix elements are defined as follows:

$$H_{i\alpha, j\beta} = \sum_{A=1}^{N_i^{\text{type}}} \sum_{A'=1}^{N_j^{\text{type}}} b_i^{(A)} b_j^{(A')} h_{i\alpha, j\beta}^{(A, A')} \quad (3)$$

with β representing the atomic orbital β of atom type A' at site j , and $h_{i\alpha, j\beta}^{(A, A')}$ the original off-diagonal Hamiltonian element for the case of atom

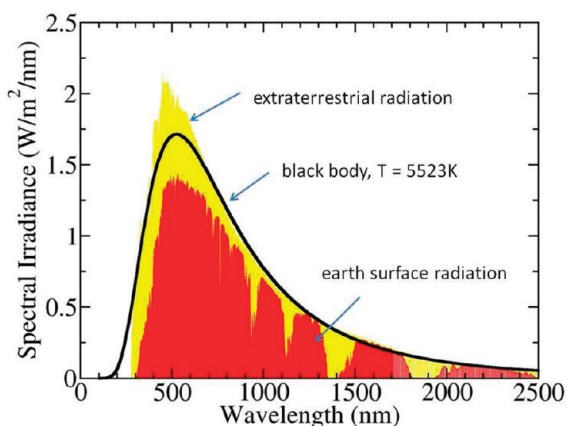


Figure 2. Solar spectrum and approximation based on the radiance of a blackbody at 5523 K.

type A at site i , and atom type A' at site j :

$$h_{i\alpha, j\beta}^{(A, A')} = K' S_{i\alpha, j\beta}^{(A, A')} (h_{i\alpha, i\alpha}^{(A)} + h_{j\beta, j\beta}^{(A')})/2 \quad (4)$$

where $K = 1.75$ and $K' = K + \Delta^2 + \Delta^4(1 - K)$ is defined according to the original Wolfsberg–Helmholz formula,³² with $\Delta = (H_{i\alpha, i\alpha}^{(A)} - H_{j\beta, j\beta}^{(A')}) / (H_{i\alpha, i\alpha}^{(A)} + H_{j\beta, j\beta}^{(A')})$. The off-diagonal overlap matrix elements $S_{i\alpha, j\beta}^{(A, A')}$ for atom types A at site i and atom types A' at site j are defined as follows:

$$S_{i\alpha, j\beta} = \sum_{A=1}^{N_{\text{type}}} \sum_{A'=1}^{N_{\text{type}}} b_i^{(A)} b_j^{(A')} S_{i\alpha, j\beta}^{(A, A')} \quad (5)$$

The participation coefficients are initialized randomly. These coefficients are subsequently optimized with respect to the property of interest (i.e., solar light absorption) computed from the solar spectrum and the oscillator strengths of allowed transitions obtained, using elements $h_{i\alpha, i\alpha}^{(A)}$, $h_{j\beta, j\beta}^{(A')}$ and $h_{i\alpha, j\beta}^{(A, A')}$ as defined for the original EH Hamiltonian, where the STO parameters reported by Hoffmann et al.³² are used without any further corrections. The STO basis set includes 3d, 4s, and 4p atomic orbitals for Ti, 2s and 2p atomic orbitals for O, C, and N elements, and 1s orbital for H.

2.2. Extended Hückel TB-LCAP Optimization of Photoabsorption. The participation coefficients of the reference structure are randomized and subsequently optimized to maximize the photoabsorption probability:

$$f_{\text{sum}} = \sum_{p, q} f_{pq} \times P(\lambda_{pq}) \quad (6)$$

defined as the sum of products of the oscillator strengths f_{pq} of electronic state transitions $q \leftarrow p$, with the transition wavelengths λ_{pq} , times the probability of harvesting a solar photon with such a wavelength:

$$P(\lambda) = I(\lambda) = \frac{8\pi hc}{\lambda^5} \frac{1}{e^{hc/\lambda kT} - 1} \quad (7)$$

as modeled by the spectral radiation of a blackbody at $T = 5523$ K (see Figure 2).

The oscillator strength f_{pq} corresponds to the transition between electronic eigenstates $|\psi_p\rangle$ and $|\psi_q\rangle$:³³

$$f_{pq} = 8 \frac{\pi^2 \nu_{pq} c m_e}{3 h e^2} |\mu_{pq}|^2 \quad (8)$$

where ν_{pq} is the transition frequency in cm^{-1} , c is the speed of light in vacuum, m_e is the electron mass, h is the Planck constant, e is the electron charge, and $\mu_{pq} = \langle \psi_q | r | \psi_p \rangle$ is the transition dipole moment.

For pure states (i.e., states with participation coefficients equal to either 1 or 0), the transition dipoles $\mu_{pq} = \langle \psi_q | r | \psi_p \rangle$ are obtained in terms of the tight-binding extended Hückel eigenstates $|\psi_q\rangle = \sum_i \alpha Q_{i\alpha}^q |\phi_{i\alpha}\rangle$ and $|\psi_p\rangle = \sum_{j\beta} \beta Q_{j\beta}^p |\phi_{j\beta}\rangle$ in the basis set of atomic STO's $|\phi_{i\alpha}\rangle$, where α represents the type of atomic orbital, i labels the atomic site, and $Q_{i\alpha}^q$ is the expansion coefficient obtained by solving the eigenvalue problem, introduced by eq 1, giving:

$$\mu_{pq} = \sum_{i, \alpha} \sum_{j, \beta} Q_{i\alpha}^q Q_{j\beta}^p \langle \phi_{i\alpha} | r | \phi_{j\beta} \rangle \quad (9)$$

For alchemical states (i.e., with $0 \leq b_i^{(A)} \leq 1$), the generalized atomic orbitals are

$$|\phi_{i\alpha}\rangle = \sum_{A=1}^{N_{\text{type}}} \sqrt{b_i^{(A)}} |\phi_{i\alpha}^{(A)}\rangle \quad (10)$$

giving generalized transition dipoles by substituting eq 10 into eq 9:

$$\mu_{pq} = \sum_{i, \alpha} \sum_{j, \beta} Q_{i\alpha}^q Q_{j\beta}^p \left[\sum_{A=1}^{N_{\text{type}}} \sum_{A'=1}^{N_{\text{type}}} \sqrt{b_i^{(A)}} \sqrt{b_j^{(A')}} \langle \phi_{i\alpha}^{(A)} | r | \phi_{j\beta}^{(A')} \rangle \right] \quad (11)$$

where elements $\langle \phi_{i\alpha}^{(A)} | r | \phi_{j\beta}^{(A')} \rangle$ are calculated using the STO atomic basis set.³³ Substituting eq 11 into 8, and then eq 8 into 6, we obtain the total “photoabsorption” of the alchemical structure with participation coefficients $0 \leq b_i^{(A)} \leq 1$.

The total photoabsorption cross section is maximized with respect to the participation coefficients using standard optimization techniques (e.g., the quasi-Newton BFGS algorithm),³⁴ computing the gradients of the photoabsorption probability using standard finite difference expressions:

$$\frac{\partial f_{\text{sum}}}{\partial b_j} = \frac{f_{\text{sum}}(b_1, b_2, \dots, b_j + \delta, \dots, b_n) - f_{\text{sum}}(b_1, b_2, \dots, b_j - \delta, \dots, b_n)}{2\delta} \quad (12)$$

To obtain structures that maximize the probability of solar light harvesting, the sum over electronic state transitions introduced in eq 6 must include all allowed transitions in the UV–visible–IR region where the solar radiance has significant intensity. For photoconversion, however, it is important to maximize photoabsorption due to electronic transitions that yield IET (e.g., the adsorbate electron is excited to the adsorbate LUMO, mixed with electronic states in the semiconductor conduction band, and cross-transits directly into electronic states in the conduction band). For example, the phenyl-acac HOMO–LUMO transition has been shown to yield ultrafast IET into the TiO₂ surface. Hence, the inverse design of chromophores based on the phenyl-acac reference structure is focused on the optimization of photoabsorption by maximization of $f_{\text{HL}} \times P(\lambda_{\text{HL}})$. Here, f_{HL} and $P(\lambda_{\text{HL}})$ are computed using eqs 7 and 6, respectively, for $p = \text{HOMO}$ and $q = \text{LUMO}$. It is important to note, however, that the problem of improving the overall efficiency of solar energy conversion depends not only on the efficiency of photoabsorption but also on the kinetics and efficiency of interfacial electron injection, charge carrier collection, and hole transport to the counterelectrode. Therefore, optimizing photoabsorption by inverse design addresses one of the multiple aspects that determine the overall efficiency of energy conversion.

2.3. TDDFT Spectra and Simulations of Interfacial Electron Transfer. The most promising structures obtained by optimization of participation coefficients at the EH/TB-LCAP level are subsequently analyzed through calculations of photoabsorption spectra at the TDDFT level of theory and the simulations of interfacial electron injection dynamics, as in previous work.^{5,6,27–29} These calculations involve geometry optimization at the DFT level, and TDDFT calculations of vertical excitations and oscillator strengths for the optimized dye molecules using the B3LYP functional³⁵ as implemented in Gaussian

03.³⁶ The basis set included the LANL2DZ basis for Ti and the 6-31G* basis for all other elements. Geometry relaxation of the dye-TiO₂ structures is performed by the DFT (PW91/GGA)³⁷ method with periodic boundary conditions using a plane-wave basis set and the ultrasoft Vanderbilt pseudopotential³⁸ approximation, as implemented in the Vienna ab initio Simulation Package (VASP/VAMP).^{39–41} The wave function cutoff is 300 eV, and single γ -point sampling is used due to the large size of the supercell.

Simulations of interfacial electron injection analyze adsorbate molecules covalently attached through the acac linkage to two Ti⁴⁺ ions on the (101) surface of TiO₂ anatase supercells (including 32 TiO₂ units). Hydrogen atoms were added to the oxygen atoms with dangling bonds on the TiO₂ surface, and the Ti⁴⁺ ions with dangling bonds (i.e., Ti⁴⁺ ions with less than 4-coordination bonds) on the anatase surface were saturated with water molecules to eliminate artificial surface states.

The photoexcited electron is assumed to be initially localized in the adsorbate LUMO, and the time-evolved electronic wave function $|\Phi(t)\rangle$ is obtained as a linear combination of atomic orbitals:

$$|\Phi(t)\rangle = \sum_{i\alpha} B_{i\alpha}(t) |\phi_{i\alpha}\rangle \quad (13)$$

where the time-dependent expansion coefficients $B_{i\alpha}(t)$ are calculated, as follows:

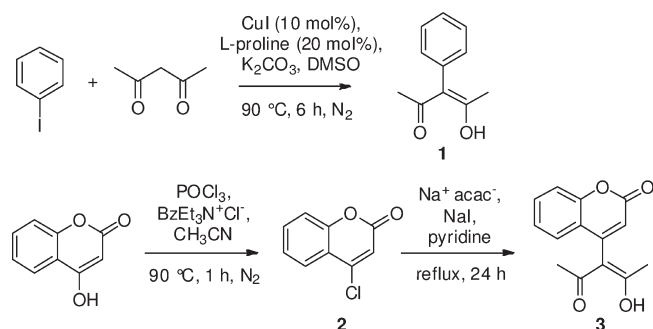
$$B_{i\alpha}(t) = \sum_q C_q Q_{i\alpha}^q e^{-(i/\hbar)E_q t} \quad (14)$$

where C_q are the expansion coefficients of initial wave function $|\Phi(0)\rangle = \sum_q C_q |\psi_q\rangle$ in the basis set of eigenvectors $|\psi_q\rangle$. The time-scale for electron injection is obtained from the decay of the survival probability, for the electron in the adsorbate molecule, as follows:

$$P(t) = \left| \sum_{i,\alpha} \sum_{j,\beta} B_{i\alpha}^*(t) B_{j\beta}(t) S_{i\alpha,j\beta} \right| \quad (15)$$

where $S_{i\alpha,j\beta} = \langle \phi_{i\alpha} | \phi_{j\beta} \rangle$. Here, indices i and α label only atoms in the adsorbate molecule, while indices j and β run over all atoms in the nanostructure.

2.4. Synthesis Procedure and UV–Vis Characterization. All reagents were purchased from Aldrich and used without further purification. The ¹H NMR spectra were obtained using a Bruker spectrometer operating at 500 MHz. Phenyl-acac (**1**) was synthesized according to a literature procedure.⁴² The molecules 4-chlorocoumarin (**2**) and 4-acac-coumarin (**3**) were synthesized according to a modified literature procedure, as follows:⁴³



4-Chlorocoumarin (2). A solution of 4-hydroxycoumarin (0.730 g, 4.5 mmol) and benzyltriethylammonium chloride (4.101 g, 18 mmol) in acetonitrile (17 mL) was stirred at 40 °C for 10 min. Phosphorus oxychloride (1.9 mL, 20 mmol) was added dropwise over 5 min, and the resulting solution was stirred at 40 °C for 30 min, then heated at 90 °C for 1 h under N₂. After removal of solvent, 16.5 mL of deionized water

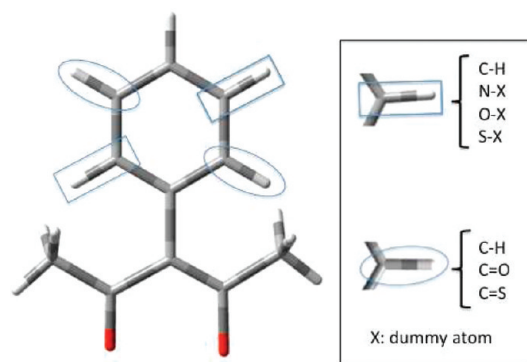


Figure 3. Phenyl-acac reference molecular framework implemented for maximization of $f_{\text{HL}} \times P(\lambda_{\text{HL}})$, using the EH/TB-LCAP inverse design method. The square and oval boxes highlight the parts of the molecular framework optimized by inverse design, as a linear combination of the atomic sites listed in the inset.

was added, and the solution was stirred at room temperature for 3 h. The resulting yellow precipitate (**2**) was filtered and dried under vacuum overnight (0.604 g, 74.3% yield). ¹H NMR (CDCl₃, 500 MHz) δ : 7.88 (d, 1H), 7.62 (t, 1H), 7.38 (m, 2H), 6.62 (s, 1H).

4-acac-Coumarin (3). In a round-bottom flask equipped with a reflux condenser, 2,4-pentanedione (0.2 mL, 2.0 mmol) was added dropwise over 5 min to a stirring solution of 21% sodium ethoxide in ethanol (0.75 mL, 2 mmol); stirring was continued for 3 min. The mixture was dried under vacuum to yield sodium acetylacetonate. A solution of **2** (0.216 g, 1.2 mmol) and sodium iodide (0.180 g, 1.2 mmol) in pyridine (4 mL) was cannulated into the flask, and the resulting mixture was stirred at reflux for 24 h. The cooled solution was poured over 1 N HCl and extracted with ethyl acetate. The organic layer was washed with water, then with an aqueous saturated solution of NaCl and dried over Na₂SO₄. Upon removal of solvent, the residue was purified by column chromatography on silica using a 1:1 mixture of ethyl acetate and hexane to yield **3** (0.073 g, 24.9% yield). ¹H NMR (CDCl₃, 500 MHz) δ : % enol (100%) 16.82 (s, 1H, OH), 7.59 (t, 1H), 7.43 (m, 2H), 7.30 (t, 1H), 6.37 (s, 1H).

UV–Visible Spectroscopy. All UV–vis absorption spectroscopic measurements were obtained using a Varian Cary 300 spectrophotometer. Thin films of sensitized TiO₂ were prepared, and absorption measurements of the films were obtained in diffuse reflectance geometry using an integrating sphere. To prepare the films, a suspension of P25 TiO₂ nanoparticles in deionized water was doctor bladed onto glass microscope slides, then calcined at 450 °C for 2 h. The resulting TiO₂ slides were sensitized by soaking overnight in a solution of the desired dye.

3. RESULTS AND DISCUSSION

3.1. Inverse Design. The TB-LCAP inverse design method is illustrated as applied to the reference molecular framework defined by the phenyl-acac anion (see Figure 3), a chromophore that absorbs only in the UV region (e.g., at 284 nm in methanol solution). The superposition of atom types in the six-membered ring is allowed to vary continuously as a linear combination of functional groups including atom types C, N, O, S, and H to optimize photoabsorption in the visible light region due to HOMO–LUMO transitions.

Figure 3 shows a phenyl-acac structural model, used as the reference framework for EH/TB-LCAP optimization of $f_{\text{HL}} \times P(\lambda_{\text{HL}})$. The variable atom sites that are boxed by ovals correspond to linear combinations of C–H, N–X, O–X, and S–X

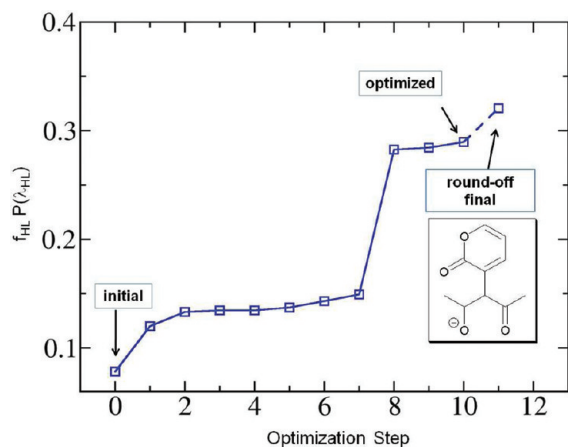


Figure 4. Typical evolution of $f_{\text{HL}} \times P(\lambda_{\text{HL}})$ associated with the HOMO–LUMO transition, as it changes during the EH/TB-LCAP optimization by modifying the phenyl-acac molecular framework, depicted in Figure 3, after randomization of participation coefficients as described in the text.

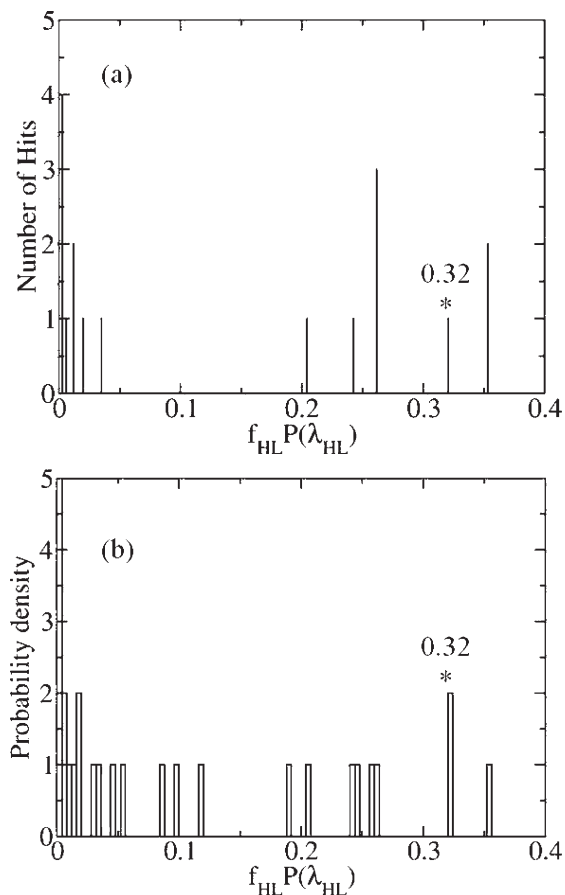


Figure 5. Results of TB-LCAP inverse design optimizations for 100 random-initial conditions, including (a) the histogram with the number of structures found with maximum $f_{\text{HL}} \times P(\lambda_{\text{HL}})$, as compared to panel (b) the normalized histogram for the enumerated 144 possible chemical structures.

(where X represents a “dummy atom”), while the sites boxed by rectangles are linear combinations of C–H, C=O, and C=S

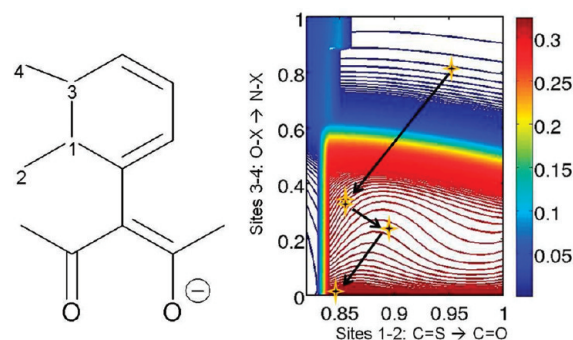


Figure 6. TB-LCAP inverse design optimization (arrows) along the hypersurface of $f_{\text{HL}} \times P(\lambda_{\text{HL}})$ represented by contour levels, as a function of participation coefficients in the range where $b_{(1-2)}^{(\text{C=O})}$ changes continuously from 0 to 1 as site (2) in the alchemical structure (left panel) changes from S to O, and $b_{(3-4)}^{(\text{N-X})}$ changes continuously from 0 to 1 as site (3) changes continuously from O to N. Starting at (0.95, 0.8), the TB-LCAP optimization rapidly converges to (0.86, 0) and yields 4 upon round-off to (1, 0).

functional groups, giving a total number of 144 possible molecules for this simple molecular framework.

Figure 4 shows a typical evolution of the property of interest (i.e., $f_{\text{HL}} \times P(\lambda_{\text{HL}})$), as it improves during the first 10 steps of TB-LCAP inverse design optimization with respect to the participation coefficients, keeping the fixed nuclear configuration as defined by the reference structure. After rounding off the participation coefficients, the final structure (step 11) is relaxed at the DFT B3LYP level of theory, yielding the optimum structure 4. The photoabsorption spectrum of 4 is then computed at the TDDFT B3LYP level and compared to the spectrum of the initial (phenyl-acac) structure to confirm the capability of the TB-LCAP inverse design as applied to the optimization of solar light absorption.

Figure 5a shows the results of optimizations for 100 random initial conditions of participation coefficients, after maximization of $f_{\text{HL}} \times P(\lambda_{\text{HL}})$. By enumerating all possible structures as defined in Figure 3 and computing $f_{\text{HL}} \times P(\lambda_{\text{HL}})$ for all those possible structures (see Figure 5b), we confirm that the inverse design method is able to identify compound 4 as the optimum structure (i.e., the structure with maximum value of the scoring function $f_{\text{HL}} \times P(\lambda_{\text{HL}})$, as computed at the TDDFT (B3LYP/6-31 g*) level). Figure 5a shows that the value of $f_{\text{HL}} \times P(\lambda_{\text{HL}})$ obtained at the EH level for structure 4 is 0.32. In addition, there is another structure with an even larger value of the scoring function ($f_{\text{HL}} \times P(\lambda_{\text{HL}}) = 0.35$). However, the latter compound is a “false” optimum because its absorption band shifts to the UV region when calculated by the TDDFT (B3LYP/6-31 g*) level. These results show that the search algorithm is effective because the EH/TB-LCAP landscape is sufficiently smooth as a function of the participation coefficients, and the gradients provide useful information for guiding the optimization.

The hypersurface of $f_{\text{HL}} \times P(\lambda_{\text{HL}})$ is a 14-dimension surface. Figure 6 analyzes the smoothness of the surface as a function of the LCAP participation coefficients, leading to the alchemical path from a random initial to structure 4. Figure 6 shows a two-dimensional contour plot for structural variation where sites 1 and 2 vary from C=S to C=O (i.e., $b^{(\text{C=O})} + b^{(\text{C=S})} = 1$), and sites 3 and 4 vary from O–X to N–X (i.e., $b^{(\text{O-X})} + b^{(\text{N-X})} = 1$). In general, the gradients of $f_{\text{HL}} \times P(\lambda_{\text{HL}})$ versus $b^{(\text{N-X})}$ and $b^{(\text{C=O})}$ (see Figure 6) are well-defined and can be used for the TB-LCAP search paths in extended regions. The alchemical

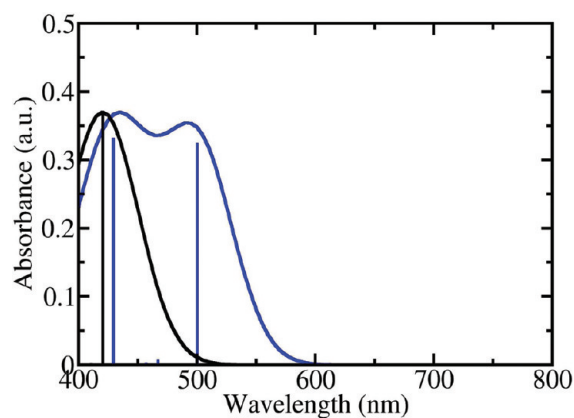


Figure 7. Photoabsorption spectra of phenyl-acac anion (black) and structure 4 (blue), calculated by the extended Hückel level of theory, as computed during the TB-LCAP optimization using the nuclear configuration of the reference (phenyl-acac) structure.

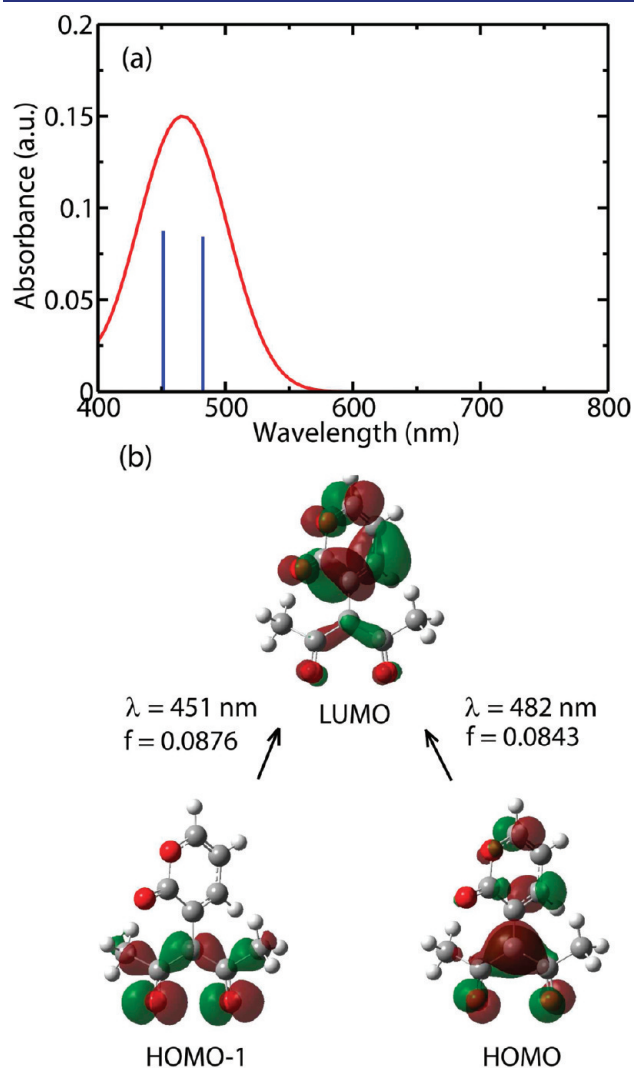


Figure 8. (a) UV-visible photoabsorption of 3-acac-pyran-2-one anion, and (b) characteristic electronic transitions calculated at the TDDFT (B3LYP/6-31G*) level. A Gaussian function with fwhm = 60 nm is used to broaden the bands and facilitate the comparison to experimental spectra with inhomogeneous broadening.

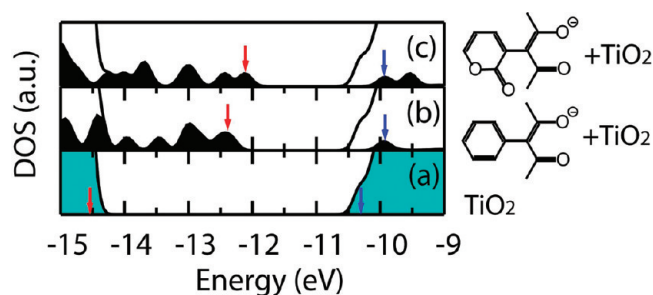


Figure 9. Density of states (DOS) calculated by the extended Hückel theory for a bare TiO_2 anatase nanostructure (a) and functionalized TiO_2 -anatase nanostructures with phenyl-acac (b) and 4 (c) adsorbed to the (101) surface of TiO_2 . The solid-black areas in (b) and (c) are the projected DOS of the adsorbate molecules. Red and blue arrows point to electronic states with a predominant contribution from the HOMO and LUMO, respectively. Bands are convoluted with a Gaussian function with fwhm = 0.1 eV to facilitate the visualization.

structures with $b^{(\text{C}=\text{O})} < 0.75$ have small values of $f_{\text{HL}} \times P(\lambda_{\text{HL}})$; the gradients are not useful for guiding the optimization. Therefore, initial conditions in that region (or in other regions with small gradients) are typically rejected, and new initial conditions are selected by randomizations of the participation coefficients. For the area with $b^{(\text{C}=\text{O})} > 0.75$, the surface shows a global trend to increase as $b^{(\text{N}^-\text{X})}$ decreases from 1 to 0, leading to successful searches. Except for a narrow area formed by $b^{(\text{C}=\text{O})} \approx 0.75\text{--}0.85$ and $b^{(\text{N}^-\text{X})} \approx 0.60\text{--}1.0$ where the LCAP search paths might be trapped, any other TB-LCAP paths with random initialization leads to structure 4 (i.e., the point with $b^{(\text{C}=\text{O})} = 1$ and $b^{(\text{O}^-\text{X})} = 1$). For example, if an optimization is initialized with $b^{(\text{C}=\text{O})} = 0.95$ and $b^{(\text{O}^-\text{X})} = 0.80$ (see Figure 6), the TB-LCAP algorithm searches along the path consisting of the points (0.86, 0.35), (0.86, 0.34), and (0.90, 0.24), and then quickly approaches (0.84, 0.01) that is very close to the convergence point (0.86, 0). Rounding off (0.86, 0) to (1, 0), we obtain structure 4.

Figure 7 shows the absorption spectrum of 4 as compared to the spectrum of phenyl-acac, calculated by the extended Hückel level, based on the nuclear configuration of the reference (phenyl-acac anion) structure. Figure 7 shows that upon TB-LCAP optimization for photoabsorption of solar light, the resulting structure includes an absorption band red-shifted toward the visible range by ~ 100 nm, as compared to the photoabsorption of the reference structure. Such a band corresponds to the HOMO–LUMO transition, localized in the 2-pyrone ring. These spectroscopic features are confirmed at the TDDFT level, as shown in the next section, indicating that the extended-Hückel calculations of oscillator strengths during TB-LCAP optimization are not only efficient but also in semiquantitative agreement with calculations at the TDDFT level.

3.2. Absorption Spectrum, Density of States, and Interfacial Electron Transfer. Figure 8 shows the photoabsorption spectrum of the 3-acac-pyran-2-one anion (4), obtained at the TDDFT (B3LYP/6-31G*) level, after geometry optimization at the DFT (B3LYP/6-31G*) level of theory. As estimated by the extended Hückel calculation for the reference (phenyl-acac) structure (Figure 7), the TDDFT photoabsorption spectrum of 4 shows two visible transitions between 400 and 550 nm. As shown by the analysis of molecular orbitals in Figure 8b, the band at 482 nm is primarily due to the LUMO←HOMO transition, while the band at 451 nm corresponds to the LUMO←HOMO–1 transition.

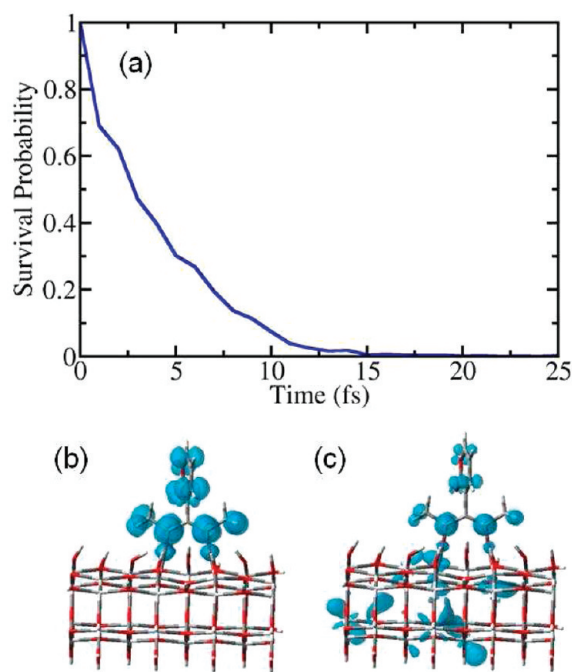


Figure 10. (a) Time-dependent electronic survival probability that at time t (fs) the electrons remains on the 3-acac-pyran-2-one adsorbate, when covalently attached to the TiO_2 -anatase (101) surface, and the isosurfaces of electronic density $t = 0$ fs (b) and at $t = 12$ fs (c), after photoexcitation to the adsorbate LUMO.

Figure 9 shows the densities of states (DOS) of a bare TiO_2 nanostructure, calculated at the extended Hückel level of theory, as compared to the corresponding DOS of the nanostructure functionalized with the reference phenyl-acac (anion) and **4**, respectively. The projected DOS onto electronic states of the adsorbates show that both adsorbates introduce additional electronic states in the TiO_2 band gap, upon adsorption to TiO_2 . In addition, Figure 9 shows that the HOMO of **4** is shifted to higher energies when compared to the HOMO of phenyl-acac (see red arrows), leading to a red-shift of the HOMO–LUMO transition frequency. The LUMO of **4** overlaps with states in the TiO_2 conduction band, and therefore has a suitable position to induce interfacial electron injection.

Figure 10 shows the time-dependent survival probability that the electron is still in the adsorbate **4** at time t , after photoexcitation of the chromophore, as described by simulations of interfacial electron transfer. Figure 10 shows that electrons initially excited to the LUMO of **4** are rapidly injected into the semiconductor nanostructure, in about 10 fs. Such ultrafast IET is ideally suited for solar photoconversion where solar radiance, rather than photoabsorption and interfacial electron transfer, should be rate limiting. The predicted IET dynamics could be probed by ultrafast laser spectroscopy, as in previous studies,^{5,6,27–29} although the calculated dynamics would correspond with experiments only when the dominant contribution to photoabsorption results from photoexcitation to the adsorbate LUMO, as determined by the energy, shape, and duration of the pulse.

3.3. Experimental Explorations. Coumarin-derived dyes^{7,9,44} are commercially available compounds formed by the same pyran-2-one ring of compound **4**, although fused to a phenyl ring at positions 5 and 6 and anchoring groups (typically $-\text{COOH}$)

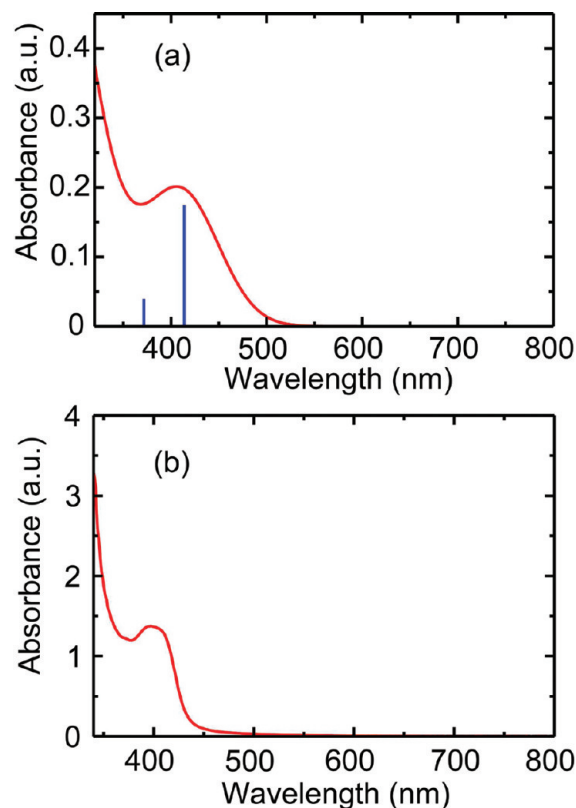


Figure 11. Photoabsorption spectra of 4-acac-coumarin anion in methanol solution calculated at the TDDFT (B3LYP/6-31G*) level, using a PCM solvation model (a), and measured experimentally in 2.0×10^{-5} M methanol solution (b). The computed absorption bands have been convoluted with a Gaussian function with $\text{fwhm} = 90$ nm to model the solution inhomogeneous broadening.

that can bind to the TiO_2 surface. Coumarin-COOH derived dyes such as C343 and NKX-2311 are synthesized by adding donor/acceptor groups or extending the π -conjugation using alkene units and have already been shown to have intense visible light absorption and fast interfacial electron injection rates at the femtosecond time scale.^{7,9} The good performance of the coumarin-derived dye-sensitizers suggests that compound **4** could be used as a lead chromophore in subsequent optimization.

To experimentally explore our computational predictions that 3-acac-pyran-2-one derivatives can absorb light at the edge of the UV–visible spectrum and lead to interfacial electron transfer into TiO_2 surfaces, we have synthesized and analyzed the 4-acac-coumarin (**3**) compound both in solutions and attached to TiO_2 surfaces. Figure 11 shows the comparison of the calculated and experimental absorption spectra of 4-acac-coumarin anion in methanol solution, where the deprotonation of **3** is experimentally induced with 1 equiv of tetrabutylammonium hydroxide. Figure 11a predicts that 4-acac-coumarin anion has an absorption band at 406 nm, in semiquantitative agreement with the experimental photoabsorption spectrum (Figure 11b) where an absorption band at 402 nm is present and is responsible for the yellowish color of the 4-acac-coumarin methanol solution.

Figure 12 compares the calculated absorption spectrum for 4-acac-coumarin (anion) adsorbed on a $[\text{Ti}_2\text{O}_2(\text{OH})_2(\text{H}_2\text{O})_4]^{2+}$ model structure (Figure 12a) to the experimental spectrum of 4-acac-coumarin adsorbed on TiO_2 thin films (Figure 12b).

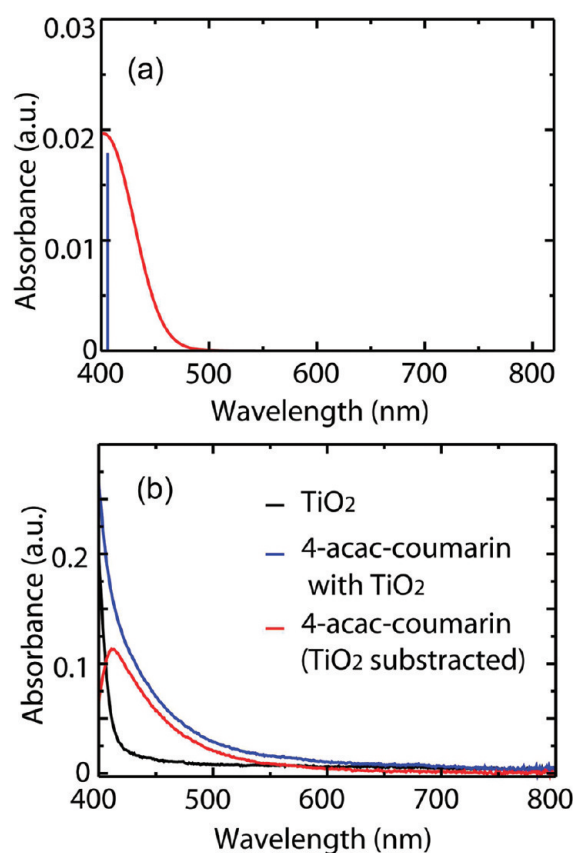


Figure 12. Photoabsorption spectra for 4-acac-coumarin adsorbed on TiO_2 : (a) calculated at the TDDFT (B3LYP/6-31G*) level for 4-acac-coumarin covalently attached to a $[\text{Ti}_2\text{O}_2(\text{OH})_2(\text{H}_2\text{O})_4]^{2+}$ model structure; (b) measured experimentally for 4-acac-coumarin covalently attached to TiO_2 thin films in air. The computed absorption bands have been convoluted with a Gaussian function with fwhm = 60 nm to model the film inhomogeneous broadening.

In agreement with experiments, the calculations predict an absorption band centered at the UV–visible edge and peaking at 405–410 nm.

Figure 13 shows the simulated electron injection dynamics for the 4-acac-coumarin (anion) adsorbed to the TiO_2 –anatase (101) surface. The electron density on the 4-acac-coumarin anion LUMO decays rapidly at a time of 15 fs (Figure 13a), as the electron is injected from the 4-acac-coumarin LUMO to the conduction band of the TiO_2 anatase surface (Figure 13b,c).

4. CONCLUSIONS

The design and synthesis of novel acac-coumarin chromophore linkers for robust sensitization of TiO_2 were assisted by the EH/TB-LCAP inverse design method, a computational approach specifically developed to find molecular chromophores with suitable properties for solar energy conversion. The underlying inverse design strategy builds upon LCAP methodologies¹⁶ and continuously transforms alchemical superposition structures in a vicinity of a reference framework to optimize solar energy conversion as estimated by the intensity of solar radiance and the absorption due to electronic transitions responsible for interfacial electron transfer. Using phenyl-acac as a reference structure, the method predicts that 3-acac-pyran-2-one is the optimum structure subject to the selected constraints. 3-acac-pyran-2-one is a novel chromophore linker related to

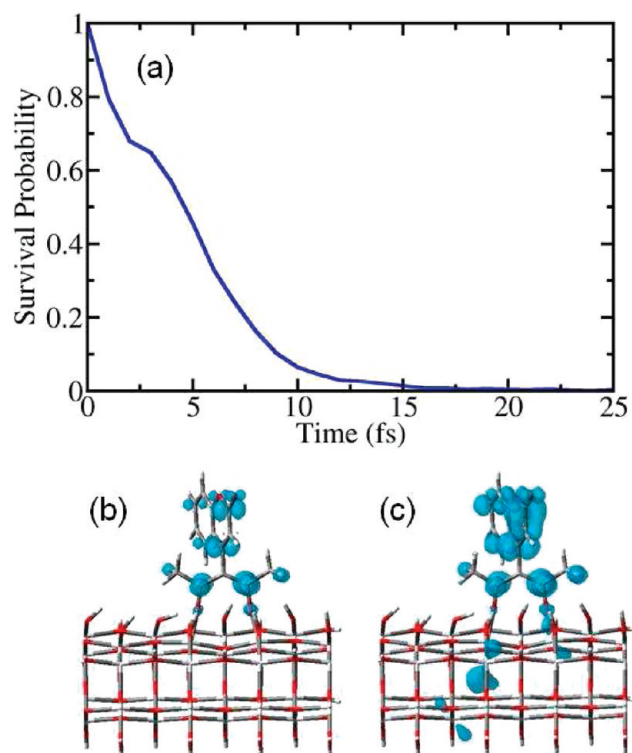


Figure 13. Interfacial electron injection from the 4-acac-coumarin LUMO to a TiO_2 anatase supercell, as simulated by the quantum dynamics propagation. The electron survival probability that at time t (fs) the electron remains on the 4-acac-coumarin LUMO decays at a characteristic time of 15 fs (a), and the snapshots of electronic charge distribution correspond to $t = 0$ fs (initial time) (b) and $t = 6$ fs (c), after initiating the interfacial electron transfer.

coumarin dyes and could be used as a lead chromophore anchor in practical applications to dye-sensitized solar cells. The synthesis and spectroscopic characterization confirms that 3-acac-pyran-2-one yields improved sensitization to solar light and provides robust attachment to TiO_2 even in aqueous conditions. These findings suggest that a variety of robust chromophore linkers could be designed by extending the 3-acac-pyran-2-one π -conjugation with alkene, donor, or acceptor groups.

■ ASSOCIATED CONTENT

S Supporting Information. Detailed TB-LCAP optimization procedures and results, the density of states analysis for the periodic dye- TiO_2 structures, the TDDFT and experimental photoabsorption spectra for phenyl-acac anion, the predicted absorption spectra and the electron injection simulation for an extended 3-acac-pyran-2-one anion using three $-\text{CH}_2=\text{CH}_2-$ units, the comparison between TDDFT and extended Hückel calculations of absorption spectra for 4-acac-coumarin anion in the gas phase and adsorbed on the TiO_2 surface, and complete ref 36. This material is available free of charge via the Internet at <http://pubs.acs.org>.

■ AUTHOR INFORMATION

Corresponding Author

dequan.xiao@yale.edu; victor.batista@yale.edu; robert.crabtree@yale.edu

■ ACKNOWLEDGMENT

This work was supported by the ANSER EFRC under U.S. DoE Award DE-PS02-08ER15944 (V.S.B. and D.X., computational) and by U.S. DoE Award 1043588 (R.H.C. and L.A.M., synthesis). V.S.B. acknowledges supercomputer time from NERSC.

■ REFERENCES

- (1) O'Regan, B.; Grätzel, M. *Nature* **1991**, *353*, 737.
- (2) Nazeeruddin, M. K.; Kay, A.; Rodicio, I.; Humphry-Baker, R.; Müller, E.; Liska, P.; Vlachopoulos, N.; Grätzel, M. *J. Am. Chem. Soc.* **1993**, *115*, 6382.
- (3) Mills, A.; Le Hunte, S. *J. Photochem. Photobiol., A* **1997**, *108*, 1.
- (4) Serpone, N. *Res. Chem. Intermed.* **1994**, *20*, 953.
- (5) Abuabara, S. G.; Cady, C. W.; Baxter, J. B.; Schmuttenmaer, C. A.; Crabtree, R. H.; Brudvig, G. W.; Batista, V. S. *J. Phys. Chem. C* **2007**, *111*, 11982.
- (6) McNamara, W. R.; Snoeberger, R. C.; Li, G.; Schleicher, J. M.; Cady, C. W.; Poyatos, M.; Schmuttenmaer, C. A.; Crabtree, R. H.; Brudvig, G. W.; Batista, V. S. *J. Am. Chem. Soc.* **2008**, *130*, 14329.
- (7) Hara, K.; Sato, T.; Katoh, R.; Furube, A.; Ohga, Y.; Shinpo, A.; Suga, S.; Sayama, K.; Sugihara, H.; Arakawa, H. *J. Phys. Chem. B* **2002**, *107*, 597.
- (8) Koumura, N.; Wang, Z.-S.; Mori, S.; Miyashita, M.; Suzuki, E.; Hara, K. *J. Am. Chem. Soc.* **2006**, *128*, 14256.
- (9) Wang, Z. S.; Cui, Y.; Hara, K.; Dan-oh, Y.; Kasada, C.; Shinpo, A. *Adv. Mater.* **2007**, *19*, 1138.
- (10) Qin, H.; Wenger, S.; Xu, M.; Gao, F.; Jing, X.; Wang, P.; Zakeeruddin, S. M.; Grätzel, M. *J. Am. Chem. Soc.* **2008**, *130*, 9202.
- (11) Bessho, T.; Zakeeruddin, S. M.; Yeh, C.-Y.; Diau, E. W.-G.; Grätzel, M. *Angew. Chem., Int. Ed.* **2010**, *49*, 6646.
- (12) Jorgensen, W. L. *Science* **2004**, *303*, 1813.
- (13) Ertl, P. *J. Chem. Inf. Comput. Sci.* **2002**, *43*, 374.
- (14) Fink, T.; Reymond, J.-L. *J. Chem. Inf. Model.* **2007**, *47*, 342.
- (15) Franceschetti, A.; Zunger, A. *Nature* **1999**, *402*, 60.
- (16) Wang, M.; Hu, X.; Beratan, D. N.; Yang, W. *J. Am. Chem. Soc.* **2006**, *128*, 3228.
- (17) Hu, X.; Beratan, D. N.; Yang, W. *Sci. China, Ser. B: Chem.* **2010**, *52*, 1862.
- (18) von Lilienfeld, O. A.; Lins, R. D.; Rothlisberger, U. *Phys. Rev. Lett.* **2005**, *95*, 153002.
- (19) von Lilienfeld, O. A. *J. Chem. Phys.* **2009**, *131*, 164102.
- (20) Dudiy, S. V.; Zunger, A. *Phys. Rev. Lett.* **2006**, *97*, 046401.
- (21) Piquini, P.; Graf, P. A.; Zunger, A. *Phys. Rev. Lett.* **2008**, *100*, 186403.
- (22) Xiao, D.; Yang, W.; Beratan, D. N. *J. Chem. Phys.* **2008**, *129*, 044106.
- (23) Hu, X.; Beratan, D. N.; Yang, W. *J. Chem. Phys.* **2008**, *129*, 064102.
- (24) Keinan, S.; Hu, X.; Beratan, D. N.; Yang, W. *J. Phys. Chem. A* **2006**, *111*, 176.
- (25) Hu, X.; Hu, H.; Beratan, D. N.; Yang, W. *J. Comput. Chem.* **2010**, *31*, 2164.
- (26) Hu, X.; Beratan, D. N.; Yang, W. *J. Chem. Phys.* **2009**, *131*, 154117.
- (27) Rego, L. G. C.; Batista, V. S. *J. Am. Chem. Soc.* **2003**, *125*, 7989.
- (28) Abuabara, S. G.; Rego, L. G. C.; Batista, V. S. *J. Am. Chem. Soc.* **2005**, *127*, 18234.
- (29) Rego, L. G. C.; Abuabara, S. G.; Batista, V. S. *J. Chem. Phys.* **2005**, *122*, 154709.
- (30) Hoffmann, R. *Rev. Mod. Phys.* **1988**, *60*, 601.
- (31) Burdett, J. K. *Chemical Bonding in Solids*; Oxford University Press: Oxford, 1995.
- (32) Ammeter, J. H.; Bürgi, H. B.; Thibeault, J. C.; Hoffmann, R. *J. Am. Chem. Soc.* **1978**, *100*, 3686.
- (33) Calzaferri, G.; Rytz, R. *J. Phys. Chem.* **1995**, *99*, 12141.
- (34) Rao, S. S. *Optimization Theory and Application*, 2nd ed.; Halsted: New York, 1978.
- (35) Lee, C.; Yang, W.; Parr, R. G. *Phys. Rev. B* **1988**, *37*, 785.
- (36) Frisch, M. J.; et al. *Gaussian 03*, revision D.02; Gaussian, Inc.: Wallingford, CT, 2004.
- (37) Perdew, J. P. In *Electronic Structure of Solids*; Ziesche, P., Eschrig, H., Eds.; Akademie Verlag: Berlin, 1991.
- (38) Vanderbilt, D. *Phys. Rev. B* **1990**, *41*, 7892.
- (39) Kresse, G.; Furthmüller, J. *VASP/VAMP*; University of Vienna: Vienna, Austria, 2001.
- (40) Kresse, G.; Furthmüller, J. *J. Comp. Mater. Sci.* **1996**, *6*, 15.
- (41) Kresse, G.; Furthmüller, J. *Phys. Rev. B* **1996**, *54*, 11169.
- (42) Jiang, Y.; Wu, N.; Wu, H.; He, M. *Synlett* **2005**, *18*, 2731.
- (43) Checchi, S.; Pecori Vettori, L.; Pinzauti, S. *Gazz. Chim. Ital.* **1969**, *99*, 501.
- (44) Alibabaei, L.; Kim, J. H.; Wang, M.; Pootrakulchote, N.; Teuscher, J.; Di Censo, D.; Humphry-Baker, R.; Moser, J. E.; Yu, Y. J.; Kay, K. Y.; Zakeeruddin, S. M.; Grätzel, M. *Energy Environ. Sci.* **2010**, *3*, 1757.